Bulletin of the Seismological Society of America, Vol. 81, No. 5, pp. 1660–1693, October 1991

FAULTING GEOMETRY AND SLIP FROM CO-SEISMIC ELEVATION CHANGES: THE 18 OCTOBER 1989, LOMA PRIETA, CALIFORNIA, EARTHQUAKE

By Grant A. Marshall, Ross S. Stein, and Wayne Thatcher

Abstract

Leveling surveys conducted before and after the Loma Prieta earthquake provide observations of the co-seismic elevation changes. These data are used to determine the faulting geometry and distribution of slip, considering planar, listric, and negatively listric fault shapes. Both the planar and nonplanar models produce elevation changes consistent with the observations. Most of the observed elevation changes can be modeled with a rupture surface that extends from 4- to 15-km depth. If the rupture surface is planar, the observations require 2.4 m of right-lateral strike slip and 1.7 m of reverse slip on a 34-km-long plane that dips 60°SW. The best-fitting model faults lie above and to the southwest of the aftershock zone. A significantly better fit to the observations is obtained when these fault geometries are allowed to have two rake values, with a larger thrust component northwest of the epicenter and a larger strike-slip component southeast of the epicenter. When a low-modulus layer over a half-space is used for consistency with the seismic *P*-wave velocity structure, the fault deepens, coming within 3 km of the hypocenter, but still locates several kilometers southwest of most aftershocks.

Introduction

Precise geodetic-leveling surveys conducted both before and after the Loma Prieta earthquake (18 October 1989; $M_s = 7.1$) provide observations of the co-seismic elevation changes. Although no active program of vertical-deformation monitoring via leveling has been pursued along this segment of the San Andreas fault zone, previous leveling surveys employed for topographic-control and land-subsidence studies have been used together with postseismic releveling to construct the co-seismic elevation changes. Station separation for more than half of this extensive network of vertical-control bench marks is about 1 km. In addition, Global Positioning System (GPS) vector observations provide limited estimates of the vertical deformation associated with the earthquake (Lisowski *et al.*, 1990). These three measurements, however, do not sufficiently describe the vertical-deformation field.

In this study, we focus on the broad-scale pattern of vertical deformation and its interpretation in terms of fault geometry and slip. Simple uniform-slip elastic-dislocation models are used to approximate the rupture surface at depth. The modeled rupture surface is then compared with seismologic, geologic, and other geodetic observations.

Data

Leveling Network

The leveling network circumscribes the southern Santa Cruz Mountains and encloses most of the aftershock zone (Fig. 1). The network spans 15 to 20 km

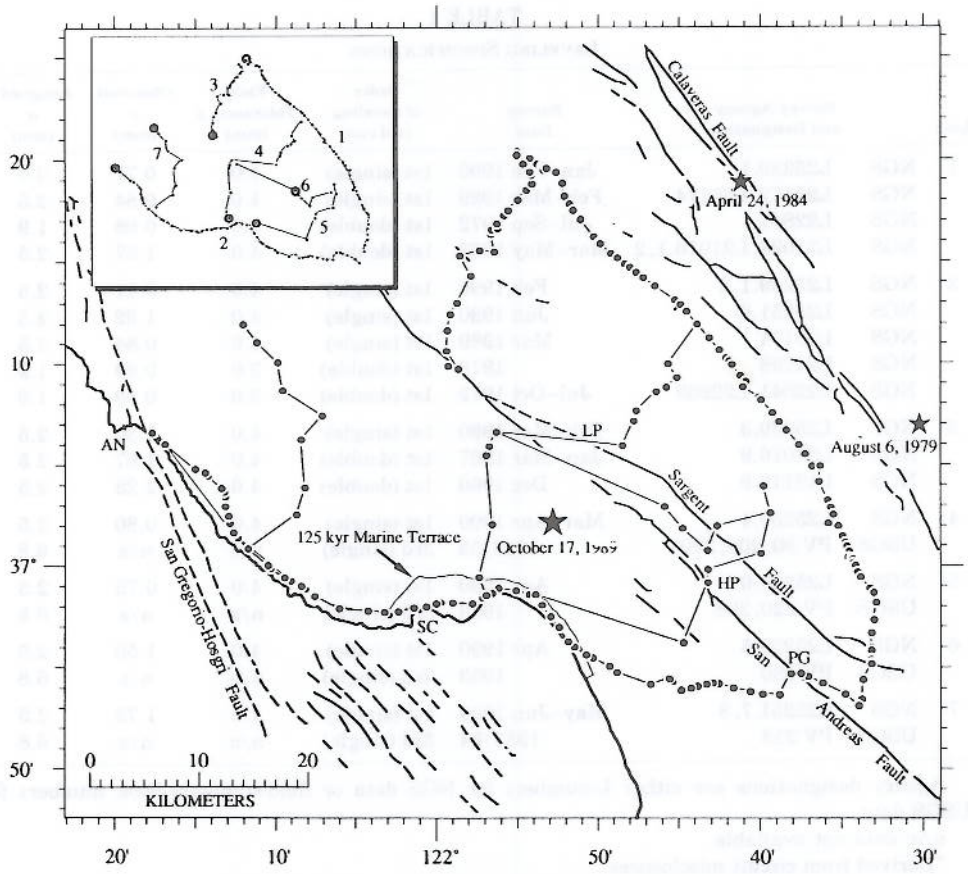

FIG. 1. Schematic map of Loma Prieta area, California, showing leveling network of 211 bench marks. Inset shows locations of lines 1 to 7; circled bench marks indicate zero-distance points in profiles shown in Figure 7. Stars: epicenters of Loma Prieta (18 October 1989; M_s = 7.1), Coyote Lake (6 August 1979; M_s = 5.9), and Morgan Hill (24 April 1984; M_L = 6.1) earthquakes. Quaternary faults from Jennings (1975). AN: Año Nuevo; SC: Santa Cruz; LP: Loma Prieta peak; HP: Hecker Pass; PG: Pajaro Gap.

(one hypocentral depth) on each side of the San Andreas fault and 67 km along strike. Postseismic surveys were chosen to give maximum coverage of the aftershock zone and the region of expected vertical deformation. The leveling routes cross the San Andreas fault in four places and the Sargent fault in three places. The network has been divided into seven lines (inset, Fig. 1), each oriented approximately parallel or perpendicular to the San Andreas fault.

Preearthquake leveling surveys were performed by both the National Geodetic Survey (NGS) and the U.S. Geological Survey (USGS) between 1948 and 1989. Postearthquake surveys were conducted from February through June 1990. We treat all of the vertical deformation occurring between the preearthquake and postearthquake surveys as "co-seismic" and attributable to the earthquake, noting that little postseismic slip was observed between October 1989 and June 1990 (Behr *et al.*, 1990; Langbein, 1990). Specifications for all the leveling surveys used in this report are listed in Table 1. First-order double-run leveling is conducted to the highest standards; third-order single-run leveling is the least precise.

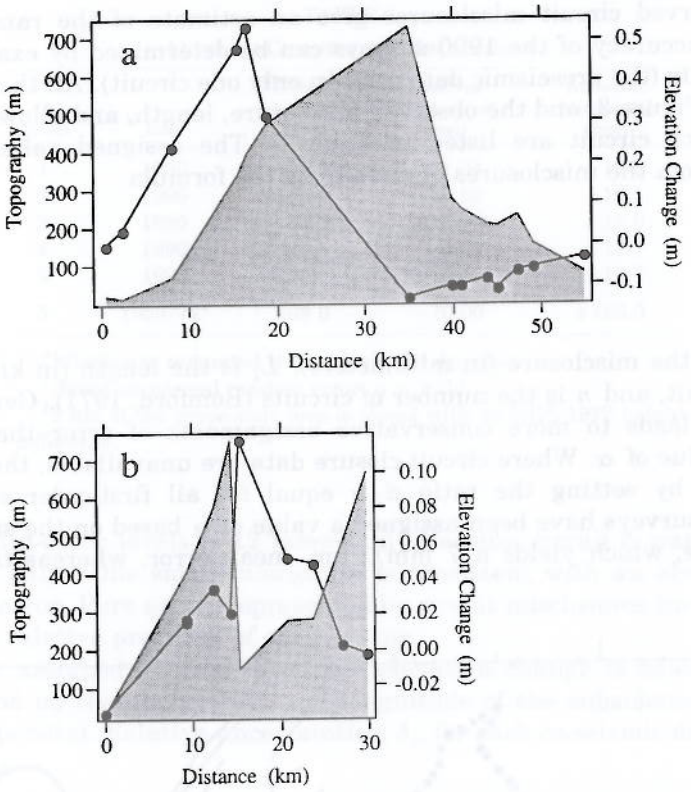

FIG. 2. Profiles of topography (left axis, shaded area) and co-seismic elevation change (right axis, dots). (a) Line 4, (b) line 7. No consistent positive or negative correlation between topography and elevation change is observed.

not show a correlation between the tilt of elevation change and topographic slope. No such correlations could be recognized in the other co-seismic data, although errors $\leqq$ 100 mm would be difficult to detect in the presence of large tectonic deformation.

Random error can be gauged from the height difference between adjacent bench marks when they are double-run (leveling in both directions) and from circuit misclosures. Random error accumulates with the square root of distance, expressed as $\alpha\sqrt{L}$, where α (units, $\mathrm{mm}/\sqrt{\mathrm{km}}$) is computed from several double-run sections and L is the length of each section (in kilometers). The observed values of α listed in Table 1 are derived from the statistics of all double-run sections and have been normalized to a distance of 1 km. If random errors are normally distributed, then $\alpha \approx 1/3\beta$, where the field tolerance, β, is the maximum allowable discrepancy between the forward and backward runs of each double-run section. If this field tolerance is not met, the section must be rerun until the forward and backward runs agree to within the tolerance. In practice, arithmetic means of several runs are used for final elevation differences when the field tolerance cannot be met after several attempts. In most cases, $\alpha < 1/3\beta$ because the errors are not normally distributed or because the number of double-run sections used to compute α is small.

We have assigned values of α to each survey based on observed circuit misclosures. In the absence of large blunders or length-dependent systematic

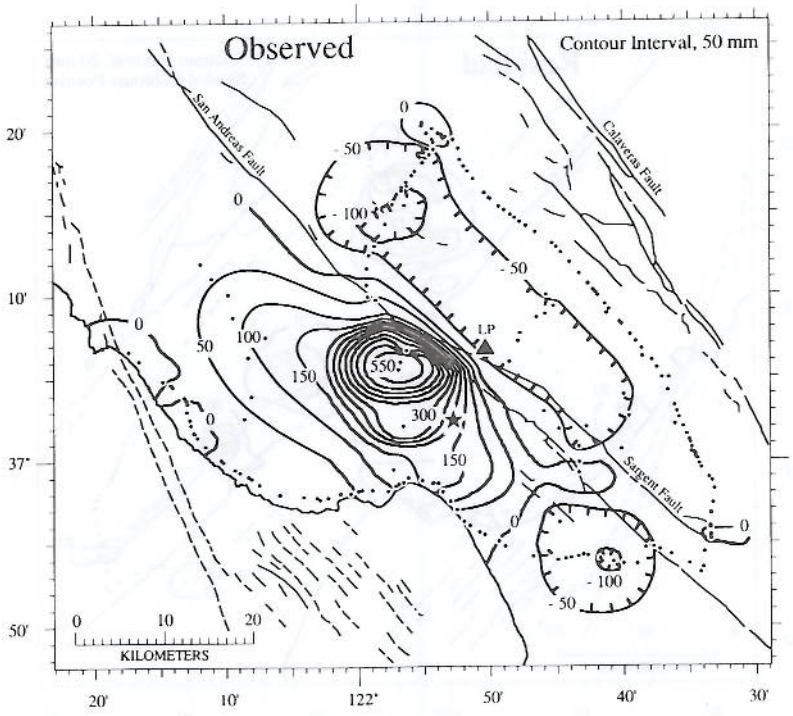

(a)

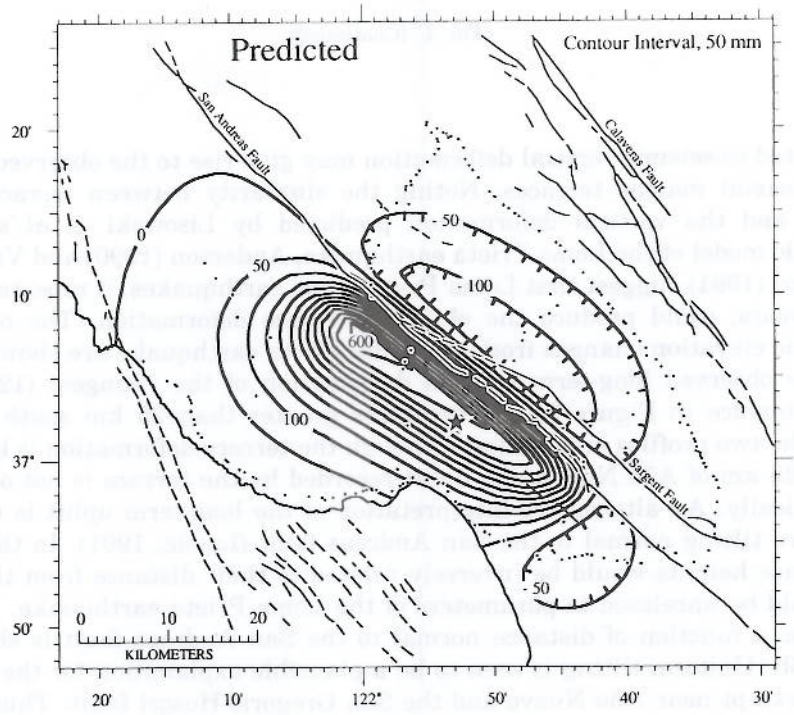

(b)

FIG. 4. Schematic map of Loma Prieta area, California, showing contours of observed (a), predicted (b), and residual (c) (observed minus predicted) co-seismic elevation change. Predicted and residual elevation changes are shown for single-rake planar model fault in Table 5. Star: epicenter of Loma Prieta earthquake (18 October 1989; M_s = 7.1). Triangle (a): Loma Prieta peak. Dots: bench mark locations.

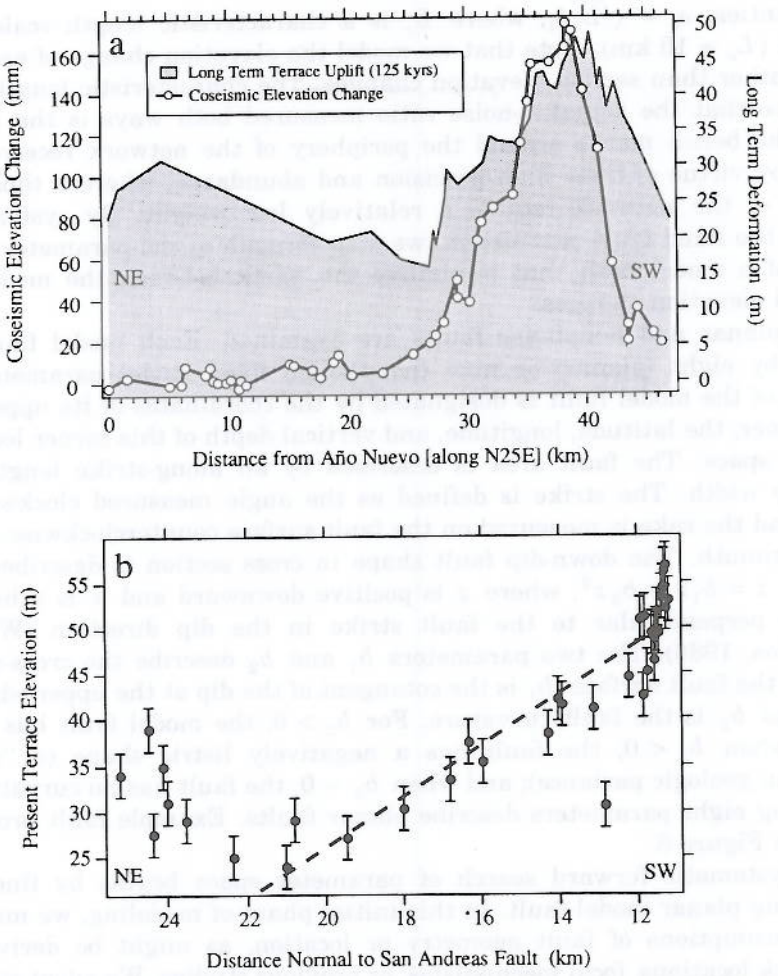

FIG. 5. (a) Profiles of co-seismic (left axis, dots) and long-term (right axis, shaded) coastal deformation. Long-term deformation derived from 125 kyr marine terrace. Profiles projected along N25E from Año Nuevo. (b) Terrace elevation as a function of perpendicular distance from San Andreas Fault. Dashed line shows linear fit excluding the first seven data points.

San Gregorio-Hosgri fault remain unexplained, and this may be due to dip-slip motion on this fault.

ANALYSIS

Modeling Elevation Changes

To model the observed co-seismic elevation changes, we describe the earthquake rupture as a superposition of moment-tensor point sources buried within a uniform elastic half-space (Ward and Barrientos, 1986; Barrientos *et al.*, 1987). The model-fault geometry and source parameters are fixed; the uniform slip is defined by a least-squares inversion. A constant elevation-change offset is also determined by inversion. In this weighted inversion, the data are weighted by the square of the observed errors, σ_o, which are proportional to the relative

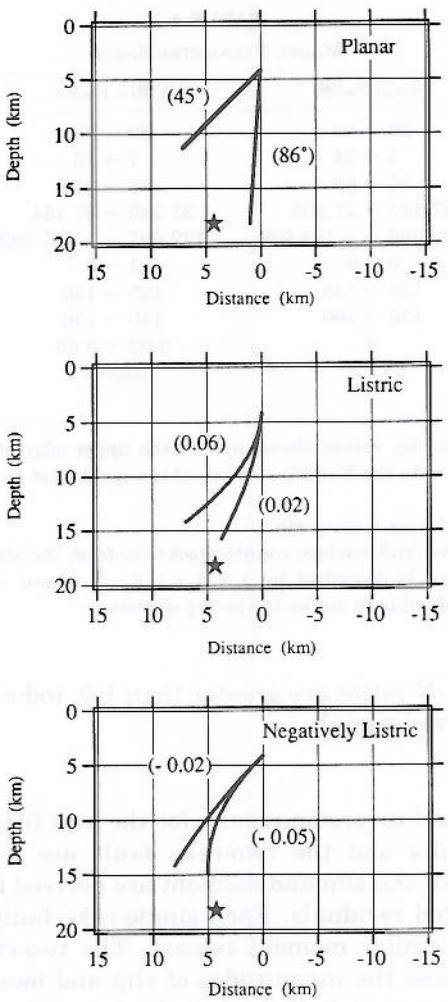

FIG. 6. Examples of planar and nonplanar fault shapes. For planar faults, minimum and maximum dips are shown; for nonplanar faults, minimum and maximum curvatures are shown. Upper-edge dip of nonplanar faults is 85° for listric shape and 45° for negatively listric shape. Star: hypocentral location relative to strikeline. Downdip fault widths are arbitrary. Complete ranges of parameters tested are listed in Table 4.

misfits are characterized by a misfit-to-noise ratio (M/N) computed as

$$\mathrm{M/N} = \left(\frac{1}{N - N_f} \sum_i^N \left(\frac{\Delta H_o - \Delta H_c}{\sigma_o} \right)_i^2 \right)^{1/2}, \tag{5}$$

where ΔH_o is the observed elevation change, ΔH_c is the calculated elevation change, σ_o is the observed error, N is the number of bench marks, and N_f is the number of fixed model parameters. If a model fits the observations to within the noise level of the data, then $\mathrm{M/N} \leq 1.0$. Our best-fitting single-rake fault has an M/N ratio of 1.61, and the segmented two-rake fault has an M/N ratio of

TABLE 5

BEST-FITTING MODELS

	Fixed Parameters										Inversion Results			
Fault Style	Length Along Strike (km)	Width Down Dip (km)	Dip, Upper Edge (°)	Dip, Lower Edge (°)	Latitude,* Northwest Corner (°)	Longitude,* Northwest Corner (°)	Depth, Upper Edge (km)	Strike† (°)	Rake‡ (°)	b_2§ (km^{-1})	Distance¶ to hypocenter (km)	Slip (m)	Moment (10^{19} N · m)	M/N ratio
Planar	34	9	60	60	37.161	−122.013	4	128	145	0.000	6	2.9 ± 0.1	2.9 ± 0.1	1.62
Listric	34	11	75	45	37.159	−122.014	4	127	143	0.040	5	2.4 ± 0.1	2.9 ± 0.1	1.67
Negatively listric	34	6	51	72	37.159	−122.021	5	127	142	−0.045	8	4.3 ± 0.1	2.8 ± 0.1	1.61
Two-rake planar	37#	9	62	62	37.164	−122.014	4.5	128	116/163**	0.000	6	2.1 ± 0.1	2.2 ± 0.1	1.33

*The vertical projection, onto the Earth's surface, of the northwest corner of the upper edge of the fault.

†Strike is measured clockwise from north.

‡Rake is measured on the fault surface counterclockwise from the strike azimuth.

§The downdip fault shape is described by $x = b_1 z + b_2 z^2$, where z is the depth and x is the horizontal distance perpendicular to strike in the dip direction.

¶Distance of closest approach between the fault surface and the hypocenter as located by Dietz and Ellsworth (1990).

The two-rake fault is segmented halfway along strike; each segment is 17 km long.

**The first rake value applies to the northwest segment, and the second to the southeast segment.

TABLE 6

ACCEPTABLE RANGES

Fixed Parameters	Planar Faults	Listric Faults	Negatively Listric Faults
Length (km)	32 → 35	30 → 35	31 → 35
Width (km)	9 → 11	7 → 12	6 → 10
Dip* (°)	57 → 60	66 → 85	48 → 55
Latitude† (°)	37.153 → 37.167	37.147 → 37.172	37.148 → 37.169
Longitude† (°)	−122.023 → −122.003	−122.031 → −121.997	−122.027 → −121.998
Depth (km)	4 → 5	4 → 6	4 → 5
Strike‡ (°)	126 → 129	125 → 130	126 → 129
Rake§ (°)	139 → 147	140 → 150	140 → 150
b_2¶ (km^{-1})	0	0.020 → 0.060	−0.045 → −0.020
Number of models	641	200	90
Inversion Results	**Planar Faults**	**Listric Faults**	**Negatively Listric Faults**
Distance to hypocenter (km)	5 → 7	4 → 7	6 → 8
Slip (m)	2.3 → 3.0	2.1 → 4.2	2.5 → 4.6
Moment ($N \cdot m \times 10^{19}$)	2.6 → 3.0	2.6 → 3.4	2.6 → 3.1
M/N	1.62 → 1.70	1.67 → 1.75	1.61 → 1.69

*For nonplanar faults the dip values shown are for the upper edge of the fault surface.

†The vertical projection, onto the Earth's surface, of the northwest corner of the upper edge of the fault.

‡Strike is measured clockwise from north.

§Rake is measured on the fault surface counterclockwise from the strike azimuth.

¶The downdip fault shape is described by $x = b_1 z + b_2 z^2$, where z is the depth and x is the horizontal distance perpendicular to strike in the dip direction.

model fit on hypocentral distance for the planar faults is illustrated in Figure 8. The best-fitting faults do not pass through the main-shock hypocenter. The best-fitting fault that passes within 1 km of the mainshock is listric and has an M/N ratio of 2.54, whereas the best-fitting single-rake fault has an M/N ratio of 1.61.

The two-rake fault significantly improves the fit by reducing the M/N ratio from 1.61 to 1.33. Although we have added two new degrees of freedom to the model, the improvement in fit is significant above the 99% confidence level. We have followed the method of Barrientos *et al.* (1987, 1989) to analyze the significance of this improvement in fit. The geometry of the two-rake fault is only slightly changed from that of the single-rake fault. The dip is slightly greater at 62°, the depth of burial is 4.5 km, and the length is 37 km. The segment lengths are equal (18.5 km each) and have rakes of 116° in the northwest and 163° in the southeast. The two-rake fault is illustrated in Figure 9.

Finally, we examined the systematic bias inherent in the use of an elastic half-space in lieu of more realistic earth structure. Eberhart-Phillips *et al.* (1990) have shown that there is a marked velocity gradient with depth in the southern Santa Cruz Mountains. Seismic *P*-wave velocities in the uppermost 3 to 5 km are 3.2 to 5.6 km/sec, increasing to 6.5 to 6.8 km/sec below 10 to 15 km. Reches and Zoback (1990) argue that strain is concentrated in the low-modulus layer. To test whether the modulus contrast caused by the velocity

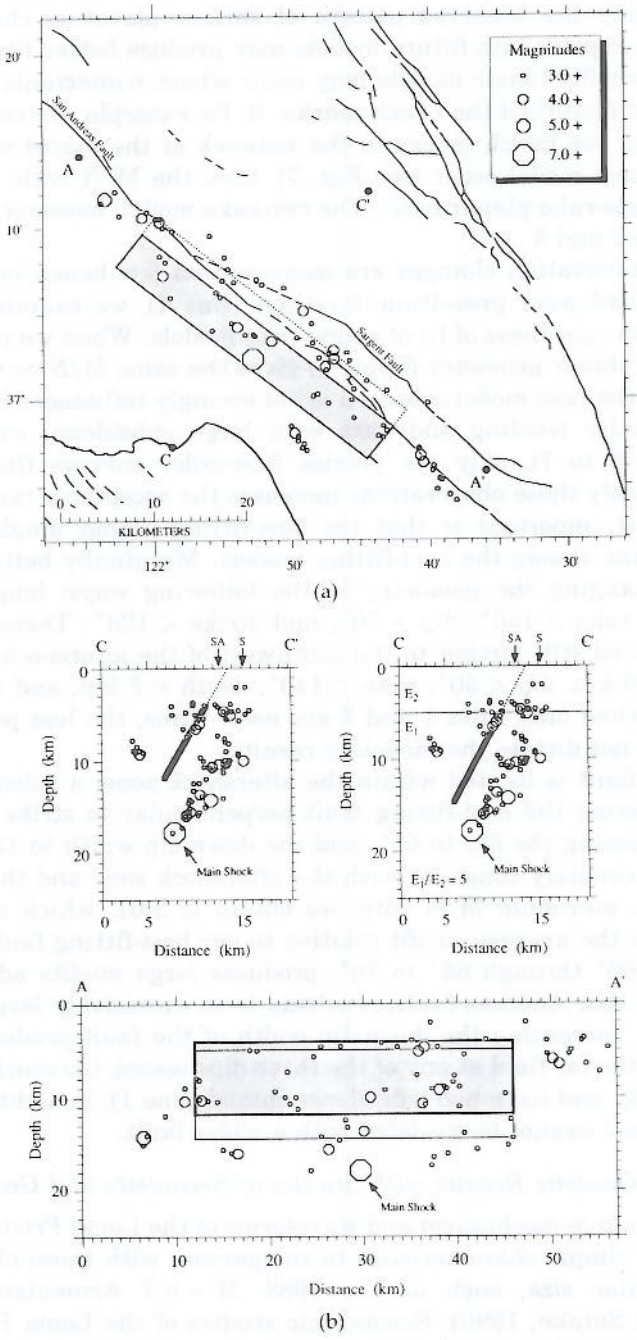

FIG. 10. Schematic map of Loma Prieta area, California, showing locations of aftershocks ($M \geq 3$) (Dietz and Ellsworth, 1990) and vertical projection of best-fitting planar model fault. Dotted line: updip projection. Cross sections C-C′ show updip projection (dotted) and locations of the San Andreas (SA) and Sargent (S) faults. Left-hand C-C′ section shows results for elastic half-space; right-hand C-C′ section shows corrections for layer over half-space. Section A-A′ shows along-strike projection of fault plane (shaded, elastic half-space; outline, layer over half-space).

TABLE 7
SOURCE STUDIES

Strike* (°)	Dip (°)	Rake† (°)	Moment (10^{19} N · m)	Depth‡ (km)	Data	Reference
120–140	**55–85**	**125–155**		18	*P*-wave first motions	Oppenheimer (1990)
122–138	**60–80**	**115–145**		19	*P*-wave first motions	Plafker and Galloway (1989)
130	73	**146**	**2.8**	18	Body waves	Barker and Salzberg (1990)
125–135	**60–70**	**135–145**	2.0–2.2	**12–16**	Body waves	Choy and Boatwright (1990)
117–127	**53–63**	**139–149**	2.1–2.4	**8**	Body waves	Langston *et al.* (1990)
126–130	61–65	127–131	**3.0–3.1**	**11–12**	Body waves	Nábělek (1990)
126	66	138	1.7	**10**	Body waves	Romanowicz and Lyon-Caen (1990)
132–144	71–81	110–130	1.5–2.5	**10–12**	Body waves	Ruff and Tichelaar (1990)
125–129	70–75	**130–144**	**2.5–3.0**	**15**	Body and surface waves	Kanamori and Satake (1990)
122–132	61–71	127–137	**2.8–3.8**	20	Surface waves	Romanawicz and Lyon-Caen (1990)
125–135	65–75	**130–140**	**2.9–3.9**	**12–122**	Surface waves	Zhang and Lay (1990)
136	70	**142–147**	**2.6–3.4**	**11**	Horizontal deformation	Lisowski *et al.* (1990)
126–129	57–60	139–147	2.6–3.0	8	Vertical deformation	This study

Bold values are consistent with our acceptable values shown at the bottom.
*Strike is measured clockwise from north.
†Rake is measured on the fault surface counterclockwise from the strike azimuth.
‡For *P*-wave studies, the depth listed indicates the rupture-initiation depth; centroidal depths are listed for body- and surface-wave studies; average depths are listed for geodetic studies; and consistency is determined by using a 4-km radius for the centroidal depths.

rake that fall within our acceptable model range: the first-motion mechanisms of Plafker and Galloway (1989) and Oppenheimer (1990), and the body-wave inversions of Choy and Boatwright (1990) and Langston *et al.* (1990). Of the 10 studies, five provide a fault dip and moment consistent with our acceptable model range, and most agree with our values of strike and rake. The seismologic determination of the source dip is least consistent with our results. The seismic studies yield a range in dip of 53° to 85°, and several studies have solutions with dips $\geq 70°$, a value that produces significant misfits to the leveling observations. Seismic values of the fault rake, which range from 110° to 155°, also exceed our acceptable model range.

Seismic moments derived from surface-wave analyses (Romanowicz and Lyon-Caen, 1990; Zhang and Lay, 1990) and from the body-wave solutions of Kanamori and Satake (1990), Nábělek (1990), and Barker and Salzberg (1990) agree with the calculated geodetic moment. Seismic moments derived from data of different frequencies and from different studies vary by a factor of as much as 2.

The consistency between the seismic and geodetic results can be addressed further by examining the spatial relation between the geodetically determined fault surface and the mainshock and its aftershocks. Dietz and Ellsworth (1990)

Page, 1984). This domain is characterized by southwest-dipping faults and northwest-trending folds. At the surface, the fault features indicate both strike-slip and reverse displacements. The surface projection of model faults compatible with the vertical geodetic data could match either the Sargent or the San Andreas fault.

Relation to Other Geodetic Studies

A geodetic model (Lisowski *et al.*, 1990) derived from precise electronic distance measurements (EDM), GPS vectors, and very long baseline interferometry (VLBI) observations is not fully consistent with our best-fitting model fault (Table 7). Lisowski *et al.* (1990) modeled the offsets in the relative positions of geodetic stations, using an elastic dislocation, and determined the source mechanism: strike = 136°, dip = 70°, rake = 144°, moment = 3.0×10^{19} N · m. The rake and moment of their solution are consistent with our results, whereas the strike and dip do not fall within our acceptable model range. Their model has a strike slightly different from that of the aftershock zone, producing a close fit to the aftershocks in the northwest and a misfit of about 2 km in the southeast. Although their model agrees better with the location of the aftershocks, it produces an M/N ratio of 2.4. Using the parameters found by Lisowski *et al.* (1990) to model the observed elevation changes produces an M/N ratio twice as large as for our best-fitting model. Likewise, our model doubles the average misfit of their observations. Future studies that combine both geodetic data sets are needed to find the fault geometry and source mechanism that are most consistent with all of the observations.

Conclusions

Observations of co-seismic elevation changes associated with the Loma Prieta earthquake favor a rupture surface extending from 4- to 15-km depth, with an average dip of 60°. Displacement on this rupture surface is composed of 2.4 m of right-lateral strike slip and 1.7 m of reverse slip. A significant improvement in fit is obtained when the segment of the fault northwest of the epicenter has a rake of 116° and the segment southeast of the epicenter has a rake of 163°. Thus, the segment northwest of the mainshock exhibited nearly pure reverse-slip motion, while the southeast segment underwent largely strike slip.

The rupture surface determined by modeling the co-seismic elevation changes lies $\approx$ 3 km southwest of most aftershocks and the mainshock hypocenter. Aftershock focal mechanisms are heterogeneous and dissimilar to the mainshock mechanism, however, suggesting that the rupture surface may be distinct from the aftershock zone. Seismic waveform models suggest that moment release is concentrated between 9- and 16-km depth, shallower than the hypocentral, rupture-initiation depth.

The connection between this rupture surface at depth and the known faults mapped at the Earth's surface remains unclear. Because both listric and negatively listric faults are permitted by the vertical geodetic data, a connection can be inferred to either the San Andreas or the Sargent fault. Alternatively, the Loma Prieta dipping oblique thrust fault and its predecessors may cut through the near-vertical San Andreas fault at depth displacing its upper-crustal trace to the northeast within the bend. Further study of the localized anomalous elevation changes seen in some of the leveling data, along with observations of surface displacements northeast of the San Andreas fault (Haugerud and Ellen,

King, G. and M. Ellis (1990). The origin of large local uplift in extensional regions, *Nature* **348**, 689–693.

King, N. E., J. C. Savage, M. Lisowski, and W. H. Prescott (1981). Preseismic and coseismic deformation associated with the Coyote Lake, California, earthquake, *J. Geophys. Res.* **86**, 892–898.

Lajoie, K. R. (1991). Pleistocene terrace deformation, Santa Cruz Mountains: Moss Beach to Watsonville, in *Workshop on the Seismotectonic Significance of the Loma Prieta Earthquake 5/91*, Asilomar Conference Grounds, Pacific Grove, California.

Langbein, J. O. (1990). Post-seismic slip on the San Andreas fault at the northwestern end of the 1989 Loma Prieta earthquake rupture zone, *Geophys. Res. Lett.* **17**, 1223–1226.

Langston, C. A., K. P. Furlong, K. S. Vogfjord, R. H. Clouser, and C. J. Ammon (1990). Analysis of teleseismic body waves radiated from the Loma Prieta earthquake, *Geophys. Res. Lett.* **17**, 1405–1408.

Lisowski, M., W. H. Prescott, J. C. Savage, and M. J. Johnston (1990). Geodetic estimate of coseismic slip during the 1989 Loma Prieta, California, earthquake, *Geophys. Res. Lett.* **17**, 1437–1440.

Nábělek, J. (1990). Rupture process of the October 18, 1989 Loma Prieta earthquake from broadband teleseismic body waves (abstract), *Seism. Res. Lett.* **61**, 46.

Oppenheimer, D. H. (1990). Aftershock slip behavior of the 1989 Loma Prieta, California, earthquake, *Geophys. Res. Lett.* **17**, 1199–1202.

Plafker, G. and J. P. Galloway (1989). Lessons learned from the Loma Prieta, California, earthquake of October 17, 1989, *U.S. Geological Survey Circular 1045*, 48.

Poland, J. F. and R. L. Ireland (1988). *Land Subsidence in the Santa Clara Valley, California, as of 1982*, Government Printing Office, Washington D.C., 61.

Prescott, W. H., N. E. King, and G. Guohua (1984). Preseismic, coseismic, and postseismic deformation associated with the 1984 Morgan Hill, California, earthquake, in *The 1984 Morgan Hill, California Earthquake*, California Division of Mines and Geology, 137–148.

Reasenberg, P. and W. L. Ellsworth (1982). Aftershocks of the Coyote Lake, California, earthquake of August 6, 1979: a detailed study, *J. Geophys. Res.* **87**, 10637–10655.

Reches, Z. and M. D. Zoback (1990). Theoretical analysis of the deformation of a layered sequence above a fault—Preliminary application to the Loma Prieta Earthquake, *Chapter X, Stanford Rock Physics and Borehole Geophysics* **40**, Stanford University.

Romanowicz, B. and H. Lyon-Caen (1990). The Loma Prieta earthquake of October 18, 1989: results of teleseismic mantle and body wave inversion, *Geophys. Res. Lett.* **17**, 1191–1194.

Ruff, L. J. and B. W. Tichelaar (1990). Moment tensor rate functions for the 1989 Loma Prieta earthquake, *Geophys. Res. Lett.* **17**, 1187–1190.

Stein, R. S. (1981). Discrimination of tectonic displacement from slope-dependent errors in geodetic leveling from southern California, 1953–1979, in *Earthquake Prediction: An International Review*, D. W. Simpson and P. G. Richards, (Editors), American Geophysical Union, Washington, D.C., 441–456.

Stein, R. S., C. T. Whalen, S. R. Holdahl, W. E. Strange, and W. Thatcher (1986). Saugus-Palmdale, California, field test for refraction error in historical leveling surveys, *J. Geophys. Res.* **91**, 9031–9044.

Valensise, G. and S. N. Ward (1991). Long-term uplift of the Santa Cruz coastline in response to repeated earthquakes along the San Andreas Fault, *Bull. Seism. Soc. Am.* **81**, 1694–1704.

Wald, D. J., D. V. Helmberger, and T. H. Heaton (1991). Rupture model of the 1989 Loma Prieta earthquake from the inversion of strong motion and broadband teleseismic data, *Bull. Seism. Soc. Am.* **81**, 1540–1572.

Ward, S. N. and S. E. Barrientos (1986). An inversion for slip distribution and fault shape from geodetic observations of the 1983 Borah Peak, Idaho, earthquake, *J. Geophys. Res.* **91**, 4909–4919.

Zhang, J. and T. Lay (1990). Source parameters of the 1989 Loma Prieta earthquake determined from long-period Rayleigh waves, *Geophys. Res. Lett.* **17**, 1195–1198.

U. S. Geological Survey
345 Middlefield Road MS 977
Menlo Park, California 94025

Manuscript received 1 May 1991

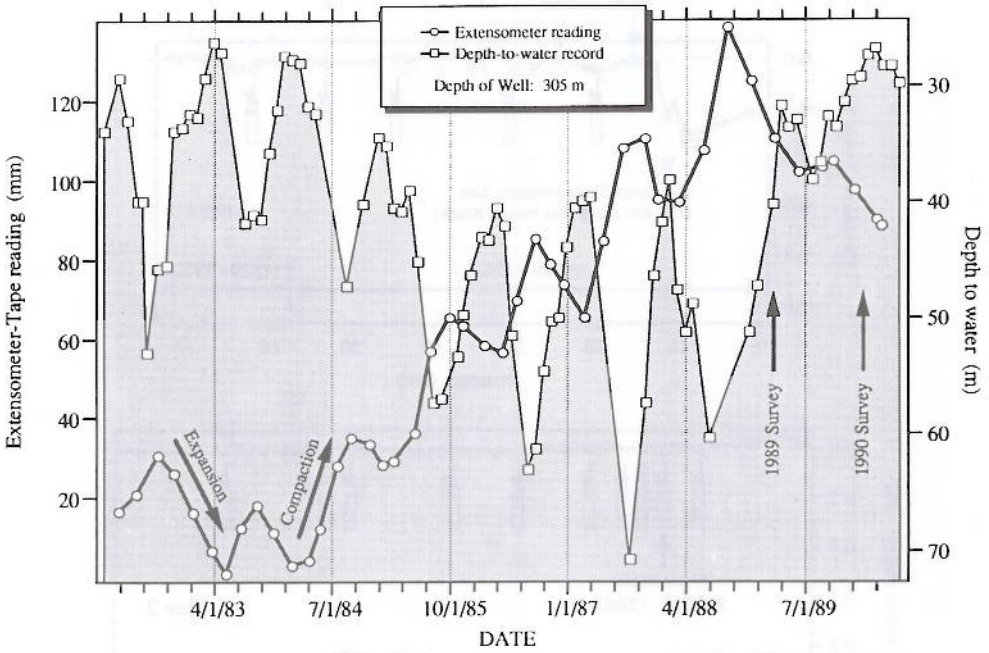

FIG. A1. Extensometer readings (left axis) and depth-to-water records (right axis) for well 7S/1E-16C11 in San Jose. Increasing readings indicate compaction, whereas decreasing readings indicate expansion of aquifer system in depth range 0 to 305 m. Note that a net expansion occurs during co-seismic interval.

basin. To correct for rate changes, the subsidence-rate functions are multiplied by a rate-correction factor, which is the ratio of the subsidence rate during the co-seismic interval to the rate during the preseismic interval. Average subsidence rates and rate-correction factors for lines 1 and 3 are listed in Table A1; these average rates are derived from the readings of the two extensometers at the San Jose site.

Depth-to-water records for wells along lines 1 and 2 were examined to assess the validity of our assumption of constant subsidence rates in the areas outside the San Jose subsidence basin. We have examined the histories of 16 wells whose locations are shown in Figure A2. The coupling of land subsidence to water-table fluctuations is not spatially uniform; except for one well, there are no large water-table fluctuations that would require a modification of the subsidence rates represented by the leveling data outside the San Jose area. Near Watsonville, well 12S/2E-15E01 has a larger ratio of subsidence to water-table decline than that observed in San Jose, possibly indicating that subsidence is particularly sensitive to the water table there. The ratio of subsidence to water-table decline, and the total water-table decline during the interval 1978 to 1989, are used to predict subsidence of the junction-point bench mark between these two preseismic surveys and thus to adjust the datum level for the preseismic survey along line 2.

Corrected co-seismic profiles for lines 1 through 3 are computed by subtracting the subsidence-correction functions from the observed-elevation-change profiles. The correction functions may not contain all the bench marks of the co-seismic survey, and so they are interpolated for missing points. Because subsidence basins and subsidence patterns determined from preseismic leveling

have primarily short spatial wavelengths, elevation-change profiles tend to be smoother after correction. Reduction of the short-wavelength components serves as a test of the efficacy of the correction. The corrections for lines 1 through 3 are all well behaved, except for the north end of line 2 between 55 and 84 km. We believe that this problem originates in the north half of the 1972 survey, where there may be a height-dependent error; thus, the subsidence correction for this area has been neglected. The observed and corrected elevation changes and the correction functions for lines 1 through 3 are plotted in Figure A3.

For the network to be self-consistent, overlapping end points of each survey line must have the same value of co-seismic elevation change. To accomplish

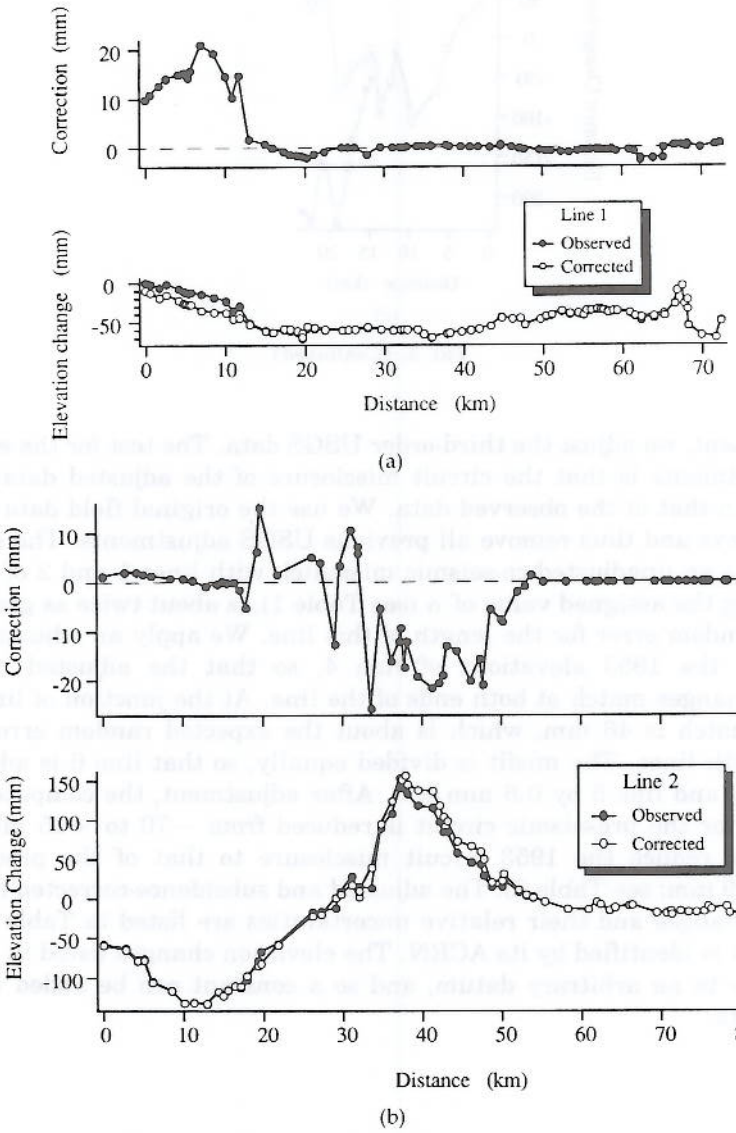

FIG. A3. Observed and corrected co-seismic elevation changes and correction functions for lines 1 (a), 2 (b), and 3 (c). Note change of scale between correction function and elevation changes for (a) and (b) but not (c).

TABLE A2

CO-SEISMIC ELEVATION CHANGES

ACRN	Survey Distance (km)	Latitude (°)	Longitude (°)	Co-seismic Elevation Change (mm)	Relative Uncertainty δ_i (mm)
Line 1:					
HS5161	0.000	37.3519	−121.9169	−9.8	4.3
HS5160	0.598	37.3489	−121.9175	−12.9	4.3
HS2886	2.598	37.3461	−121.9036	−15.6	4.5
HS5162	4.166	37.3411	−121.8958	−22.6	4.6
HS2828	4.787	37.3394	−121.8914	−26.2	4.6
HS2826	4.968	37.3381	−121.8906	−27.0	4.6
HS2825	5.086	37.3378	−121.8894	−26.9	4.6
HS2822	5.383	37.3361	−121.8894	−27.7	4.5
HS5163	5.709	37.3378	−121.8864	−27.9	4.6
HS2813	6.972	37.3344	−121.8764	−35.6	5.1
HS2814	8.568	37.3253	−121.8697	−37.8	4.9
HS2811	10.085	37.3142	−121.8678	−38.2	4.6
HS2810	10.957	37.3075	−121.8625	−45.9	4.3
HS2809	11.753	37.3022	−121.8581	−44.6	4.6
HS2806	13.031	37.2944	−121.8506	−52.9	4.0
HS2796	15.012	37.2797	−121.8364	−61.6	4.0
HS2795	15.846	37.2744	−121.8308	−62.9	4.0
HS2792	15.982	37.2736	−121.8294	−63.0	4.0
HS2789	17.378	37.2653	−121.8183	−58.7	4.0
HS2788	18.111	37.2617	−121.8114	−59.3	4.0
HS2787	19.036	37.2564	−121.8033	−61.5	4.0
HS4926	19.609	37.2533	−121.7981	−64.0	4.0
HS5164	19.615	37.2536	−121.7981	−69.1	4.0
HS2785	20.301	37.2494	−121.7917	−55.6	4.1
HS2784	21.212	37.2450	−121.7842	−57.5	4.0
HS5165	22.505	37.2381	−121.7719	−59.5	4.0
HS4141	24.649	37.2261	−121.7506	−60.6	4.0
HS2778	25.464	37.2225	−121.7450	−59.9	4.0
HS2776	26.325	37.2167	−121.7392	−59.5	4.0
HS2773	29.592	37.1942	−121.7156	−59.7	4.0
HS2769	31.084	37.1836	−121.7047	−60.3	4.0
HS2771	31.091	37.1839	−121.7047	−60.9	4.0
HS5166	32.057	37.1769	−121.6978	−59.9	4.0
HS2768	32.432	37.1744	−121.6947	−59.5	4.0
HS5167	32.881	37.1714	−121.6919	−59.9	4.0
HS2762	34.168	37.1619	−121.6831	−60.0	4.0
HS2757	34.957	37.1569	−121.6775	−65.5	4.0
HS2758	35.919	37.1525	−121.6808	−70.5	4.0
HS2759	35.930	37.1525	−121.6805	−70.4	4.0
HS2761	36.014	37.1525	−121.6805	−69.5	4.0
HS2754	37.913	37.1433	−121.6639	−65.2	4.0
HS2753	38.236	37.1411	−121.6614	−64.3	4.0
HS2751	39.739	37.1303	−121.6500	−62.6	4.0
HS5168	40.908	37.1228	−121.6428	−60.7	4.0
HS5169	41.933	37.1156	−121.6353	−59.3	4.0
HS2745	43.419	37.1031	−121.6222	−55.5	4.0
HS2743	44.781	37.0956	−121.6156	−44.7	4.0
HS2742	44.826	37.0953	−121.6156	−45.1	4.0
HS5170	46.147	37.0850	−121.6086	−46.7	4.0
HS5171	47.156	37.0853	−121.5997	−45.6	4.0
HS2738	47.740	37.0719	−121.6011	−54.0	4.0
HS2737	49.664	37.0561	−121.5922	−46.8	4.0

TABLE A2—*Continued*

ACRN	Survey Distance (km)	Latitude (°)	Longitude (°)	Co-seismic Elevation Change (mm)	Relative Uncertainty δ_i (mm)
GU2265	29.794	36.9250	−121.8444	−7.8	3.2
GU2266	31.156	36.9317	−121.8569	4.1	4.6
GU2269	32.092	36.9361	−121.8639	−11.5	3.8
GU2268	32.100	36.9361	−121.8639	−3.7	3.6
GU2273	33.700	36.9483	−121.8733	25.9	9.0
GU2276	34.877	36.9572	−121.8817	80.9	3.5
GU2277	36.273	36.9669	−121.8914	109.8	6.1
GU2279	37.317	36.9756	−121.8972	138.7	5.0
GU2281	37.958	36.9764	−121.9031	142.4	6.5
GU2282	38.207	36.9758	−121.9044	131.0	5.0
GU2283	39.528	36.9792	−121.9181	123.6	7.0
GU2285	41.374	36.9814	−121.9364	122.6	7.7
GU2286	42.225	36.9769	−121.9431	104.0	7.4
GU2290	43.234	36.9731	−121.9528	84.0	5.3
GU2289	44.452	36.9683	−121.9636	58.8	5.5
GU2291	46.234	36.9692	−121.9842	52.8	7.3
GU2294	47.406	36.9692	-121.9967	45.9	6.0
GU1941	47.786	36.9683	−122.0014	37.0	7.6
GU1944	48.822	36.9656	−122.0117	7.4	3.5
GU3223	50.089	36.9656	−122.0244	9.3	3.9
GU1945	50.331	36.9647	−122.0250	17.9	4.0
GU1954	52.171	36.9614	−122.0411	−2.2	3.1
GU1959	53.149	36.9589	−122.0511	−8.6	3.0
GU1960	53.944	36.9611	−122.0556	−12.2	3.0
GU1964	55.451	36.9622	−122.0728	−17.5	3.0
GU1970	58.303	36.9644	−122.1033	−26.4	3.0
GU1972	60.897	36.9747	−122.1300	−27.5	3.0
GU1974	61.947	36.9811	−122.1397	−17.8	3.0
GU1975	62.447	36.9833	−122.1436	−21.1	3.0
GU1976	63.587	36.9878	−122.1550	−28.5	3.0
GU1978	64.232	36.9903	−122.1617	−25.0	3.0
GU1979	66.032	36.9986	−122.1764	−22.7	3.0
HT1572	66.418	37.0011	−122.1792	−21.9	3.0
HT1567	70.723	37.0247	−122.2108	−32.1	3.0
HT1566	71.272	37.0286	−122.2144	−29.6	3.0
HT1565	71.391	37.0292	−122.2156	−33.9	3.0
HT1564	72.456	37.0372	−122.2194	−29.5	3.0
HT1563	73.464	37.0431	−122.2208	−30.7	3.0
HT1562	74.448	37.0517	−122.2244	−30.8	3.0
HT1559	75.468	37.0597	−122.2242	−29.9	3.0
HT1558	75.930	37.0636	−122.2253	−23.5	3.0
HT1557	76.345	37.0669	−122.2281	−27.0	3.0
HT1556	78.305	37.0778	−122.2428	-23.3	3.0
HT1555	78.635	37.0800	−122.2453	−31.7	3.0
HT1552	80.343	37.0833	−122.2558	−32.4	3.0
HT1547	82.141	37.1044	−122.2872	−28.5	3.0
HT1545	83.794	37.1142	−122.3006	−33.4	3.0
Line 3:					
HS3165	0.000	37.1706	−121.9889	9.1	4.0
HS3174	0.521	37.1678	−121.9786	43.6	4.0
HS3160	1.793	37.1833	−121.9908	−29.9	4.0
HS3154	4.014	37.2008	−121.9900	−45.9	4.0
HS3150	5.706	37.2147	−121.9869	−84.1	4.0
HS3145	6.958	37.2242	−121.9800	−136.0	4.0
HS3140	10.143	37.2469	−121.9653	−172.9	4.1

TABLE A2—*Continued*

ACRN	Survey Distance (km)	Latitude (°)	Longitude (°)	Co-seismic Elevation Change (mm)	Relative Uncertainty δ_i (mm)
HT3603	25.685	37.1739	−122.1694	52.1	7.0
HT3607	28.969	37.1914	−122.1908	6.7	7.0
HT3612	31.738	37.2069	−122.2053	2.0	7.0

A constant can be freely added to all elevation change observations. We invert for this constant in our modeling; for the model shown in Figure 7, a constant of 28 mm was added to all the observations.